Korean J. Chem. Eng., **31**(4), 598-610 (2014)
DOI: 10.1007/s11814-013-0282-6

pISSN: 0256-1115
eISSN: 1975-7220

Water droplet dynamic behavior during removal from a proton exchange membrane fuel cell gas diffusion layer by Lattice-Boltzmann method

Golamreza Molaeimanesh and Mohammad Hadi Akbari†

Center for Fuel Cell Research, School of Mechanical Engineering, Shiraz University, Shiraz 71348-51154, Iran
(*Received 5 October 2013 • accepted 16 December 2013*)

Abstract−A major challenge in the application of proton exchange membrane fuel cells (PEMFCs) is water management, with the flooding of electrodes as the main issue. The Lattice-Boltzmann method (LBM) is a relatively new technique that is superior in modeling the dynamic interface of multiphase fluid flow in complex microstructures such as non-homogeneous and anisotropic porous media of PEMFC electrodes. In this study, the dynamic behavior of a water droplet during removal from gas diffusion layer (GDL) of a PEMFC electrode with interdigitated flow field is simulated using LBM. The effects of GDL wettability and its spanwise and transverse gradients on the removal process are investigated. The results demonstrate great influence of wettability and its spanwise and transverse gradients on the dynamic behavior of droplets during the removal process. Although increasing the hydrophobicity of GDL results in better droplet removal, its increase beyond a critical value does not show a significant effect.

Keywords: Multiphase Flow, Water Droplet, Proton Exchange Membrane Fuel Cell, Lattice-Boltzmann Method, GDL Microstructure

INTRODUCTION

Fuel cells are efficient energy conversion devices which directly convert the chemical energy stored in a fuel into electrical energy through electrochemical reactions. Among different types of fuel cells, PEMFC has increasingly become the most promising candidate for the power source of future automotive and portable applications due to its low operating temperature, very low emissions and high power density [1]. However, further improvements in performance, durability and cost are necessary before their widespread commercial application becomes a reality. Due to the low-temperature operation of PEMFCs, the water generated by electrochemical reactions often condenses into liquid phase, flooding the catalyst layer (CL), gas diffusion layer (GDL), and gas channels (GCs) [2, 3]. Avoiding electrode flooding is of critical importance for optimal fuel-cell performance and durability [4], which makes accurate modelling of water transport in PEMFCs essential. Many numerical models from 1D to 3D, single-phase to multi-phase, microscopic scale to macroscopic scale, also isothermal or non-isothermal, have been proposed in the literature [5]. However, due to anisotropic and non-homogenous transport properties of GDLs, only pore-scale simulation techniques such as LBM and pore network method which can take into account these characteristics are able to provide an accurate prediction.

Lattice-Boltzmann method (LBM) is a relatively new technique suitable for simulating complex fluid systems, and hence has recently attracted the interest of researchers in computational mechanics. Due to its particulate nature and local dynamics, LBM has several advantages over other conventional CFD methods, especially in modelling multi-phase fluid flow in porous media, in dealing with complex boundaries, in considering non-homogeneous and anisotropic transport properties and in parallelization of the algorithm [6]. Several investigations of water transport in fuel cell electrodes have been conducted using LBM. In some of these, the liquid phase is simulated as a continuous phase to predict parameters such as permeability or capillary pressure [7-14]. In several other investigations, liquid phase is simulated as discrete droplets [15-21]. Since continuous liquid water flow in micro-pores is never observed in situ in a PEM fuel cell and, on the contrary, a series of discrete small droplets in the GDL are often observed using the environmental scanning electron microscope (ESEM) [22,23], the second group of LB simulations seem more realistic.

In the present study, the dynamic behavior of a liquid water droplet initially placed either on the GDL/micro-porous layer (MPL) interface or on the GDL/land interface of a PEMFC electrode with interdigitated flow field is investigated through LB simulations. Because the development of liquid water droplets in the GDL is started from either GDL/MPL interface, especially at high current densities or from GDL/land interface due to coolant flow through bipolar plates [24], such initial droplet positions are considered. Since one of the major parameters influencing water transport phenomenon, and therefore controlling the onset of flooding, is the wettability properties of GDL, several simulations are conducted under different GDL wettability conditions to investigate the effect of uniform and non-uniform wettability on the removal of droplets. The treatment of GDL with a highly hydrophobic material such as polytetrafluoroethylene (PTFE) is a conventional technique for mitigating GDL flooding, which normally results in non-uniform PTFE distribution [25]. In such a case, the GDL must be considered as a porous medium with non-homogeneous and anisotropic wettability. However, in just a few of the previous LB investigations the wettability of GDL was treated as being non-uniform.

†To whom correspondence should be addressed.
E-mail: h-akbari@shirazu.ac.ir

Mukherjee et al. [12] simulated water transport in an aged GDL with mixed wettability-containing 50% randomly distributed hydrophilic pores (contact angle of 80°) and 50% randomly distributed hydrophobic pores (contact angle of 140°)-through a realistic microstructural delineation and compared the results with a new GDL with only hydrophobic pores (contact angle of 140°). They observed that at similar saturation level, the liquid water distribution was quite different for the two GDLs, underscoring the influence of the wetting characteristics and interfacial dynamics on liquid water transport.

Zhou and Wu [26] investigated the liquid water configuration for six GDLs with the same carbon fiber distribution but different surface wettabilities: the first case with all the fibers being hydrophilic, the second case with all the fibers being hydrophobic, and the other four cases with hydrophobic fiber fraction of 50%, but the hydrophobic and hydrophilic regions distributed differently. They concluded that the fraction of hydrophobic fibers cannot solely describe the transportability of the liquid water through the GDL.

Hao and Cheng [8] considered a GDL with non-uniform wettability by prescribing a hydrophilic columnar subdivision along the thickness of the GDL, which is located in the middle of the reconstructed GDL. The contact angle of fibers in the hydrophilic subdivision was set at 80° corresponding to the contact angle of carbon, while the rest was set at 115° corresponding to the contact angle of pure PTFE material. The results showed that water penetrates into the GDL selectively through the hydrophilic path, in agreement with similar pore network simulation results [27,28]. Hao and Cheng [10] simulated water transport in two GDLs with different PTFE contents of 10 wt% and 30 wt% and investigated the effect of PTFE content on the drainage and imbibition processes.

In the present study, several LB simulations with and without GDL wettability gradients are conducted. These results will help to better clarify the role of GDL wettability and its spanwise and transverse gradients on the water droplet removal from a PEMFC GDL. Although in reality controlling PTFE treatment is somehow challenging at the present, the conclusions made in this study can be used to improve hydrophobic treatment of GDLs in the future.

NUMERICAL METHOD

1. LBM Framework

In recent years, the lattice-Boltzmann method (LBM) has developed into an alternative and promising numerical technique for simulating fluid flows especially when interfacial dynamics and complex boundaries are involved. Unlike conventional numerical schemes based on solving macroscopic continuum equations, LBM is based on solving mesoscopic kinetic equations simplified for a lattice. The kinetic nature of LBM has made it a powerful numerical technique with important advantages such as the linearity of transport equation (in comparison with nonlinear Navier-Stokes equations), calculation of pressure by an equation of state (in comparison with calculating pressure by solving Poisson differential equation), etc. [29].

The present numerical study is based on the Shan and Chen (SC) multi-component multi-phase lattice-Boltzmann model [30] with single relaxation time (SRT) collision operator-the famous BGK model [31]-and D2Q9 lattice scheme. In fact, several multi-component multi-phase lattice-Boltzmann models have been presented in the literature such as color model of Gunstensen et al. [32], inter-particle interaction model of Shan and Chen [30], and free energy model of Swift et al. [33]. Among the aforementioned multi-phase LB models, the SC model is widely used for its simplicity and remarkable versatility. For simulating multi-phase and multi-component fluid flows in SC model, the lattice-Boltzmann equation is solved for each component separately, while inter-particle interactions are considered by a pseudo-potential function. For component k, the lattice-Boltzmann equation, which is derived from simplification of Boltzmann equation in a lattice [34], can be expressed as

$$f_i^k(x+c_{x,i}\Delta t, y+c_{y,i}\Delta t, t+\Delta t) = f_i^k(x,y,t) + \frac{\Delta t}{\tau^k}[f_i^{k,eq}(x,y,t) - f_i^k(x,y,t)] \quad (1)$$

where f_i^k is the density distribution function (DDF) for component k in direction i, $f_i^{k,eq}$ is the equilibrium DDF for component k in direction i, (x, y) refers to 2D space position, t is time, $\vec{c}_i = (c_{x,i}, c_{y,i})$ refers to the velocity vector in direction i, and τ^k is the relaxation time of component k. Equilibrium DDF is calculated as:

$$f_i^{k,eq} = w_i \rho^k \left[1 + \frac{\vec{c}_i \cdot \vec{u}^{k,eq}}{c_s^2} + \frac{1}{2}\frac{(\vec{c}_i \cdot \vec{u}^{k,eq})^2}{c_s^4} - \frac{1}{2}\frac{\vec{u}^{k,eq} \cdot \vec{u}^{k,eq}}{c_s^2} \right] \quad (2)$$

where w_i is the weighting factor of direction i, $\rho^k = \sum_i f_i^k$ is the fluid density of component k, c_s is the speed of sound in the lattice and $\vec{u}^{k,eq}$ is the equilibrium velocity of component k, which is calculated as:

$$\vec{u}^{k,eq} = \frac{\sum_k \frac{1}{\tau^k}\sum_i f_i^k \vec{c}_i}{\sum_k \frac{1}{\tau^k}\rho^k} + \frac{\tau^k(\vec{F}_{coh}^k + \vec{F}_{adh}^k)}{\rho^k} \quad (3)$$

Here $\vec{F}_{coh}^k$ and $\vec{F}_{adh}^k$ are the fluid-fluid interaction force and fluid-solid interaction force of component k, respectively. These forces are calculated as [35]:

$$\vec{F}_{coh}^k(x,y,t) = -\psi^k(x,y,t)\sum_{j=1}^{N} G_{coh}^{kj} \sum_{i=0}^{8} w_i \psi^j(x+c_{x,i}\Delta t, y+c_{y,i}\Delta t, t)\vec{c}_i \quad (4)$$

$$\vec{F}_{adh}^k(x,y,t) = -\psi^k(x,y,t) G_{adh}^k \sum_{i=0}^{8} w_i s(x+c_{x,i}\Delta t, y+c_{y,i}\Delta t, t)\vec{c}_i \quad (5)$$

where ψ^k is the inter-particle potential function, G_{coh}^{jk} is the cohesion factor between components k and j, G_{adh}^k is the adhesion factor of component k to the wall, and s is the solid function which is a binary value function. The function s is equal to unity if the corresponding node is at the solid part, and is equal to zero if the corresponding node is at the fluid part. Running successful lattice-Boltzmann simulations depends on selecting proper values for G_{coh}^{jk}. Usually $G_{coh}^{jk} > 0$ for $k \neq j$ and $G_{coh}^{jk} < 0$ for $k = j$. The values of G_{coh}^{jk} adopted in this study are given in Table 1. Value of G_{adh}^k determines the wettability of component k. In fact, static contact angle is a function of G_{adh}^k s.

Several definitions for ψ^k have been presented in the literature [30,35,36]. In this study, the original potential function suggested by Shan and Chen [30] is used, which is defined as follows:

$$\psi^k = \rho_0^k \left(1 - \exp\left(-\frac{\rho^k}{\rho_0^k} \right) \right) \quad (6)$$

where ρ_0^k is the reference density of component k which is set equal to 2 for all components in this study.

Upon equilibrium DDF calculation, Eq. (1) is solved through collision and streaming processes which are shown in Eqs. (7) and (8), respectively:

$$f_i^k(x,y,t+\Delta t)=f_i^k(x,y,t)\left[1-\frac{\Delta t}{\tau^k}\right]+\frac{\Delta t}{\tau^k}f_i^{k,eq}(x,y,t) \tag{7}$$

$$f_i^k(x+\Delta x,y+\Delta y,t+\Delta t)=f_i^k(x,y,t+\Delta t) \tag{8}$$

To perform the streaming process in the entire computational domain, DDFs which are aligned toward the domain must be determined at the boundaries. A simple and powerful LBM boundary condition applicable for no-slip wall is called "bounce-back," which is based on the idea that particles colliding a wall in a direction will bounce back in the opposite direction [6]. In fact, this boundary condition gives LBM the ability to model fluid flow in complicated geometries such as pore space of porous media. Several versions of this boundary condition have been proposed [35]. In the current study, the well-known mid-way version in which the wall is located halfway between two neighboring grids is used. Upon calculating DDFs at every node, the macroscopic velocity and pressure can be calculated through the following equations:

$$\vec{U}=\frac{\sum_{k=1}^{N}\sum_{i=0}^{8}f_i^k\vec{c}_i}{\sum_{k=1}^{N}\sum_{i=0}^{8}f_i^k}+\frac{1}{2}\frac{\sum_{k=1}^{N}\tau^k(\vec{F}_{coh}^k+\vec{F}_{adh}^k)}{\sum_{k=1}^{N}\sum_{i=0}^{8}f_i^k} \tag{9}$$

$$P=\frac{1}{3}\sum_{k=1}^{N}\sum_{i=0}^{8}f_i^k+\frac{1}{6}\sum_{k=1}^{N}G_{coh}^{kk}\psi^k\psi^k+\frac{1}{3}\sum_{k=1}^{N}G_{coh}^{jk}\sum_{j\neq k}\psi^k\psi^j \tag{10}$$

2. Model Validation and Calibration

2-1. Droplet Test

The multi-phase lattice-Boltzmann model briefly described in the previous section was validated by the famous Laplace law through droplet test. As the law states, the pressure difference between inside and outside of a 2D circular droplet is proportional to the interfacial tension (σ) and inversely proportional to the droplet radius:

$$\Delta p=\frac{\sigma}{R} \tag{11}$$

Various droplets with different initial sizes are placed in the middle of a rectangular lattice with 200×200 nodes and with spanwise and transverse periodic boundary conditions. Inside the droplet, the initial densities are set at ρ_{air}=0.025 and ρ_{water}=5.25 and outside the droplet, the initial densities are set at ρ_{air}=2.0 and ρ_{water}=0.0. The G_{coh}^{jk}s are selected as given in Table 1. After reaching steady state, the droplet radius and pressure difference are calculated. The results are shown in Fig. 1. Clearly, the LBM results are in a very good agreement with Laplace law. The figure also indicates that σ=0.541 lm·ts^{-2} for the LB parameters shown in Table 1.

2-2. Static Contact Angle Test

When a system with two phases of liquid and gas is in contact with a solid surface, the contact angle of liquid phase is considered as the contact angle of surface. Thus, a surface is wetting or hydrophilic if the surface contact angle is less than 90°, in which liquid phase tends to spread as a film on the surface; on the contrary, the surface is non-wetting or hydrophobic if the surface contact angle is greater than 90°, in which liquid phase tends to form a droplet on the surface. As mentioned before, in SC LB model, the contact angle is a function of G_{adh}^ks. In the current study, despite the fact that G_{adh}^1 and G_{adh}^2 are two independent variables, the relation $G_{adh}^1=-G_{adh}^2$ between their values has been adopted to perform a more straightforward calibration. In this way, several simulations with different G_{adh}^1 have been conducted and the resulting contact angles versus values of G_{adh}^1 are presented in Fig. 2. In these simulations, two initially semicircular static droplets are placed on the top and bottom span-

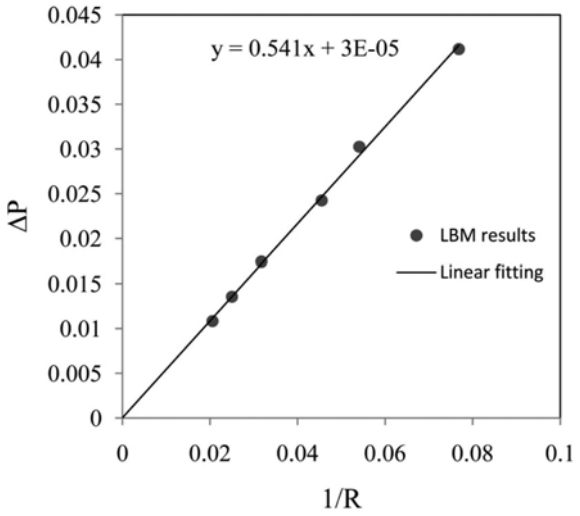

Fig. 1. Validation of LBM results of droplet test against Laplace law.

Table 1. Applied LB parameters (1: water, 2: air)

G_{coh}^{11}	G_{coh}^{12}	G_{coh}^{21}	G_{coh}^{22}
−1.85	1.27	1.27	0.0

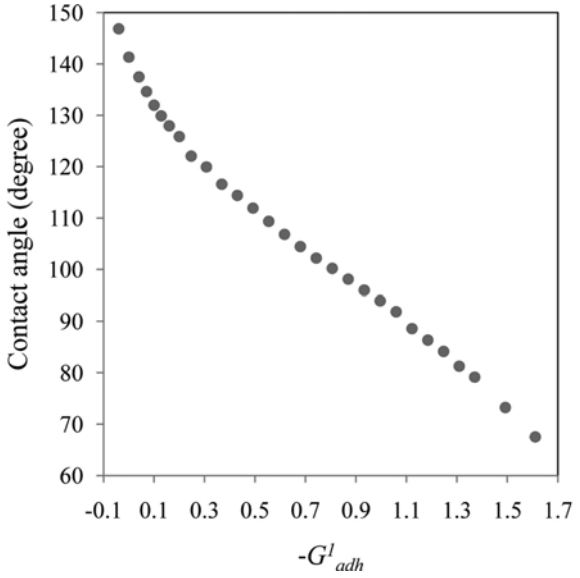

Fig. 2. LBM results of static contact angle test for calibration of G_{adh}^1.

wise solid surfaces of a rectangular lattice with 300×320 nodes. Periodic boundary conditions are applied on the left and right edges. Midway bounce-back boundary condition is applied on the bottom and top solid surfaces. The liquid phase radius is calculated through $R=(H^2+(L/2)^2)/2H$, where L is the length of liquid phase in contact with solid surface and H is the thickness of liquid phase. Upon determining R, static contact angle (θ) can be calculated through:

$$\theta=\begin{cases}\pi\text{-}\arctan\left(\dfrac{L/2}{H-R}\right), & \text{for } H>R\\ \arctan\left(\dfrac{L/2}{R-H}\right), & \text{for } H\le R\end{cases} \tag{12}$$

The resulting curve shown in Fig. 2 can be applied for the specification of G^1_{adh} and G^2_{adh} for different solid surfaces of computational domain considering their contact angles.

COMPUTATIONAL DOMAIN AND WETTABILITY DISTRIBUTION

One of the popular and efficient flow field designs for fuel cells is the interdigitated design, proposed by Nguyen [37] that has no continuous gas channels (GCs). As shown in Fig. 3(a), through a series of dead-end channel inlet fingers, air is forced into the GDL and travels under the lands into the outlet channel fingers. The two-dimensional computational domain, which is a part of a cell cross-section with an interdigitated flow field, is shown as a dashed rectangle in Fig. 3(b). It consists of half an inlet GC, half an outlet GC, as well as a land and a GDL. The bottom spanwise dashed line in this figure represents the GDL/MPL interface.

The two-dimensional GDL microstructure, which is 200 μm thick (transverse direction) and 2,000 μm long (spanwise direction), is

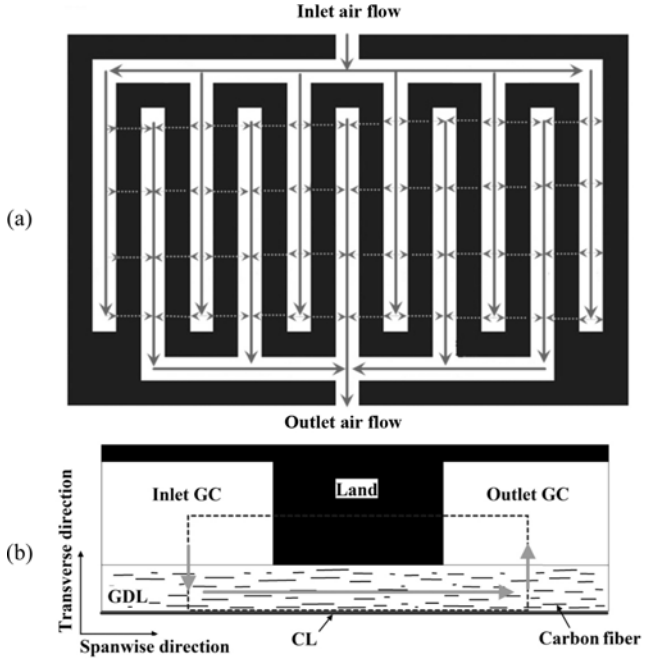

Fig. 3. A typical PEMFC electrode with interdigitated flow field: (a) top view, (b) side view.

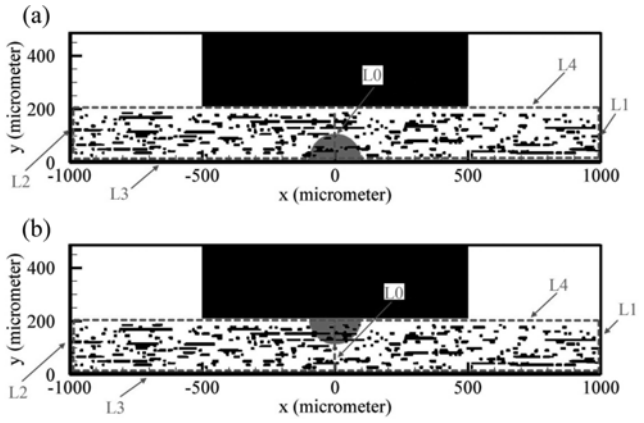

Fig. 4. GDL structure adopted from Chen et al. [17], (a) droplet initially adhered to the MPL surface, (b) droplet initially adhered to the land.

adopted from Chen et al. [17] and is shown in Fig. 4. They achieved a realistic delineation of a GDL microstructure by a stochastic reconstruction method and validated their GDL microstructure with experimental results. Although GDL microstructure can affect water transport, by adopting a realistic delineation of Chen et al. [17], its affects are taken into account implicitly in the present study only to some extent. However, direct investigation of the microstructure effects on water transport in GDL by simulating different GDLs with different microstructures can be the subject of a separate study.

The half-circles show the initial positions of the water droplets with 100 mm radius, one adhering to the MPL surface (Fig. 4(a)) and the other adhering to the land (Fig. 4(b)) as the two most possible positions where water droplets can be formed. In fact, water droplet formation is due to two main processes: generation at the cathode CL due to electrochemical reaction and condensation in cold regions. If the generated water penetrates through the MPL, it will appear on the MPL surface. Also since the coldest location during operation is generally under the lands (due to coolant flow in the bipolar plate), water will condense there first [24].

The operating condition is considered as isothermal. Air is considered as an ideal gas. Dry air with 0.5 m/s uniform velocity enters through the inlet GC and exits at 1.5 atm uniform pressure through the outlet GC. To implement inlet and outlet boundary conditions, the Zou and He [38] method is utilized. In this method when the velocity is known at a boundary and the pressure is unknown, the unknown pressure can be calculated by assuming that the non-equilibrium part of density distribution functions normal to that boundary are equal to each other. Similarly, when the pressure is known at a boundary and the velocity is not known, velocity can be calculated by the same assumption.

Symmetry boundary condition is applied for the left and right boundaries of the computational domain (transverse dashed lines in Fig. 3(b)). The no-slip condition is applied on the surfaces of all solid parts. The contact angles of the land and the MPL surfaces are assumed at 85° and 150° [39], respectively, while the contact angle of carbon fibers is not the same for all simulations or even for all fibers when a gradient of wettability is applied. More precisely, three categories of simulations are conducted. In the first category, the contact angle of GDL carbon fibers is set uniformly to a

specific value between 80° and 150°. In the second category where spanwise gradient of wettability is applied, the contact angle of GDL carbon fibers is reduced linearly from a maximum value at the transverse symmetry line (shown as L0 in Fig. 4) to a minimum value at the two transverse sides (shown as L1, L2 in Fig. 4). In the third category where transverse gradient of wettability is applied, the contact angle of GDL carbon fibers is reduced linearly from a maximum value at the spanwise bottom line (shown as L3 in Fig. 4) to a minimum value at the spanwise top line (shown as L4 in Fig. 4). The details of the last two categories are shown in Fig. 5.

Since the interfacial force acting on a water droplet trends to move it from a more hydrophobic region to a more hydrophilic one, the above-mentioned trends of wettability variation have been selected for the second and third categories. The opposite trends of wettability (increasing contact angle from L0 to L1 and L2 in the second category and from L3 to L4 in the third category) are not logically preferable, and thus have not been investigated. The main goal of this study has been to determine to what extent a spanwise or transverse wettability gradient with preferable trends can assist water removal.

After grid independency study, 1024×250 grids are used for lattice generation leading to a lattice unit of 1.953125 μm. Also every time step is set at 4.589893×10^{-8} s. Finally, a parallel FORTRAN code developed based on the proposed model is implemented for the simulations.

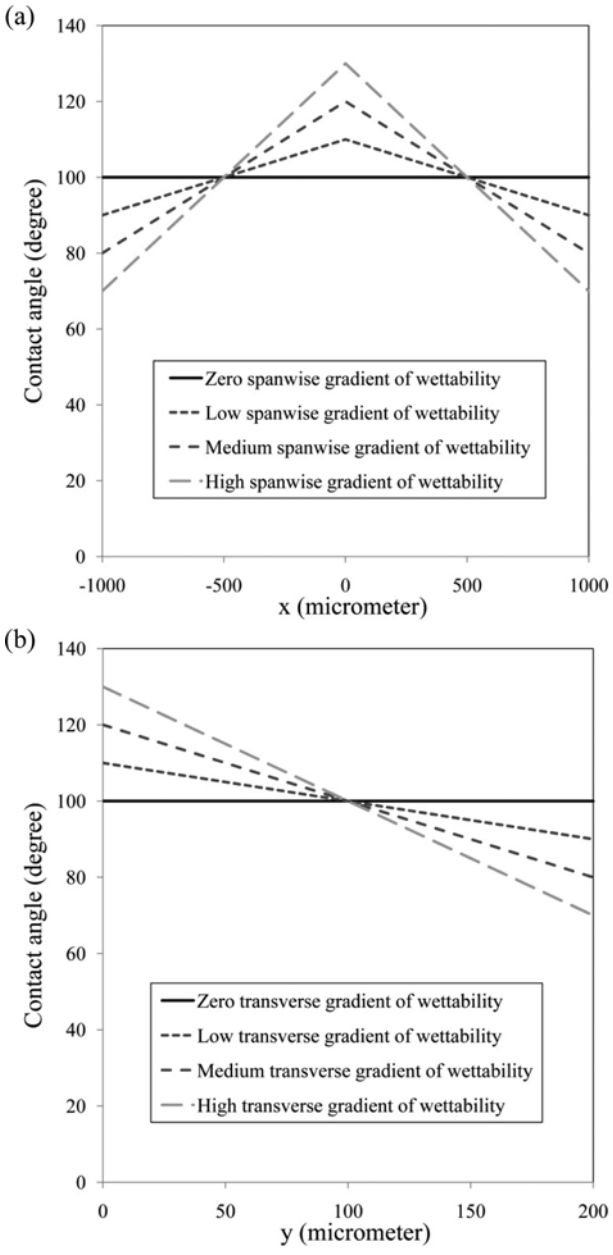

Fig. 5. GDL wettability distribution for: (a) category of simulations with spanwise gradient of wettability, (b) category of simulations with transverse gradient of wettability.

RESULTS AND DISCUSSION

1. Effect of Uniform Wettability

1-1. Droplet Initially Adhered to the MPL Surface

The GDL wettability was assumed to be uniform in the first step, hence the solid surfaces of the GDL carbon fibers are assumed to have the same contact angle. Shown in Fig. 6 is the dynamic behavior of a droplet, initially adhering to the MPL surface, during removal process through the hydrophilic GDL with contact angle of 80° (cor-

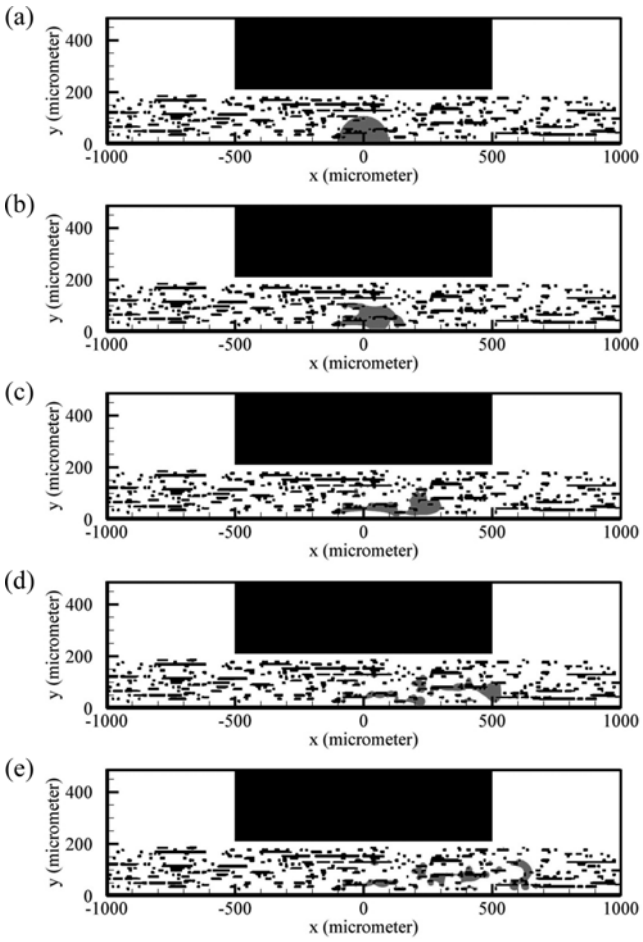

Fig. 6. Dynamic behavior of a liquid water droplet initially adhering to the MPL moving through the hydrophilic GDL with contact angle of 80° after: (a) 0 time steps, (b) 10000 time steps, (c) 20000 time steps, (d) 30000 time steps, (e) 40000 time steps.

responding to a GDL without PTFE content). It is observed that small droplets are separated from the initial droplet and stick to carbon fibers. Since these small droplets spread on the surface of carbon fibers due to their hydrophilic property, the inlet air flow can hardly move them. After about 40000 time steps (each 5000 time steps is almost 0.23 ms), the initial droplet sticks to a series of carbon fibers and will not move any further.

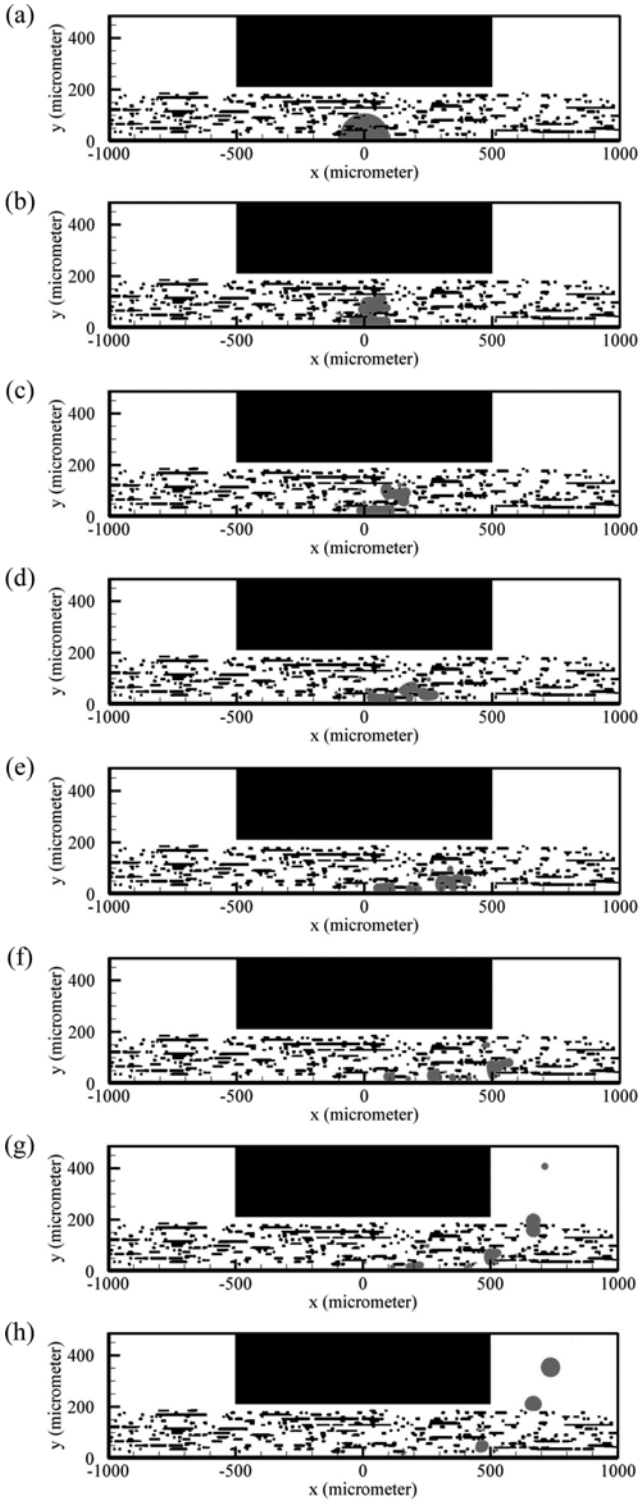

Fig. 7. Dynamic behavior of a liquid water droplet initially adhering to MPL moving through the hydrophobic GDL with contact angle of 150° after: (a) 0 time steps, (b) 5000 time steps, (c) 10000 time steps, (d) 15000 time steps, (e) 20000 time steps, (f) 25000 time steps, (g) 30000 time steps, (h) 35000 time steps.

Shown in Fig. 7 is the dynamic behavior of a droplet, initially adhering to the MPL surface, during removal process through the highly hydrophobic GDL with contact angle of 150°. Although the contact angle of pure PTFE is 115°, this simulation under such hydrophobic conditions can be helpful for future attempts to reduce GDL wettability with more hydrophobic materials. Our simulation shows that at the beginning of the droplet motion it breaks into three smaller droplets of an almost equal size. These smaller droplets, unlike in the previous case (hydrophilic GDL), will not stick to carbon fibers and easily move between them.

The time evolution of the ratio between mass of water in the GDL and the initial droplet mass adhering to the MPL, is presented in Fig. 8 for various GDL contact angles. For GDL contact angles of 80° and 90°, the droplet cannot exit the GDL; thus no sharp reduction of liquid water mass is seen for such non-hydrophobic cases. On the contrary, a sharp drop in the corresponding curve is seen for hydrophobic cases, which indicates the exit of the water droplet from the GDL. As the GDL contact angle increases, this sharp drop occurs sooner and steeper. This implies that increasing the hydrophobicity of the GDL will facilitate the removal of water droplet from the GDL and will reduce the remaining mass of liquid water in the GDL.

Examining Fig. 8 also shows that the behavior of the water droplet does not change much when contact angle is 130° to 150°. This indicates that increasing hydrophobicity beyond a critical value, 130° here, does not assist droplet removal any further. This observation is important when undesirable consequences of conventional hydrophobic treatments are considered, such as their adverse effects on the GDL gas permeability and electrical resistance [40]. In other words, increasing the contact angle of GDL beyond a critical value is not recommended. Finally, the initial slow reduction of water mass, observed in Fig. 8, is a result of the removal of water in form of

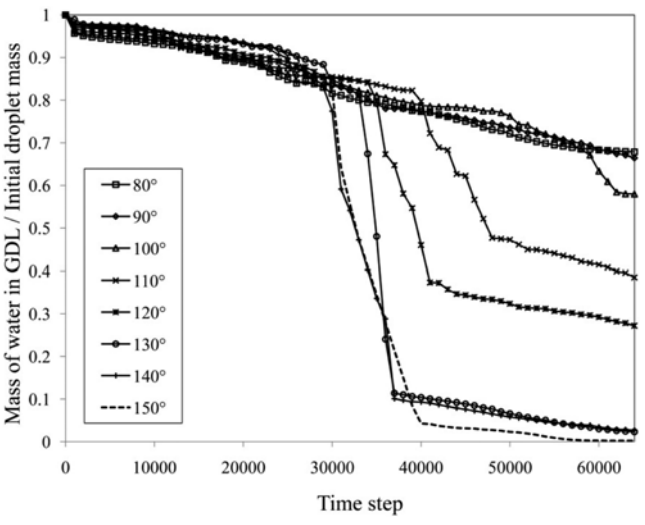

Fig. 8. The time evolution of the ratio between mass of water in the GDL and the initial droplet mass adhering to the MPL for the GDLs with uniform wettability (contact angles between 80° and 150°).

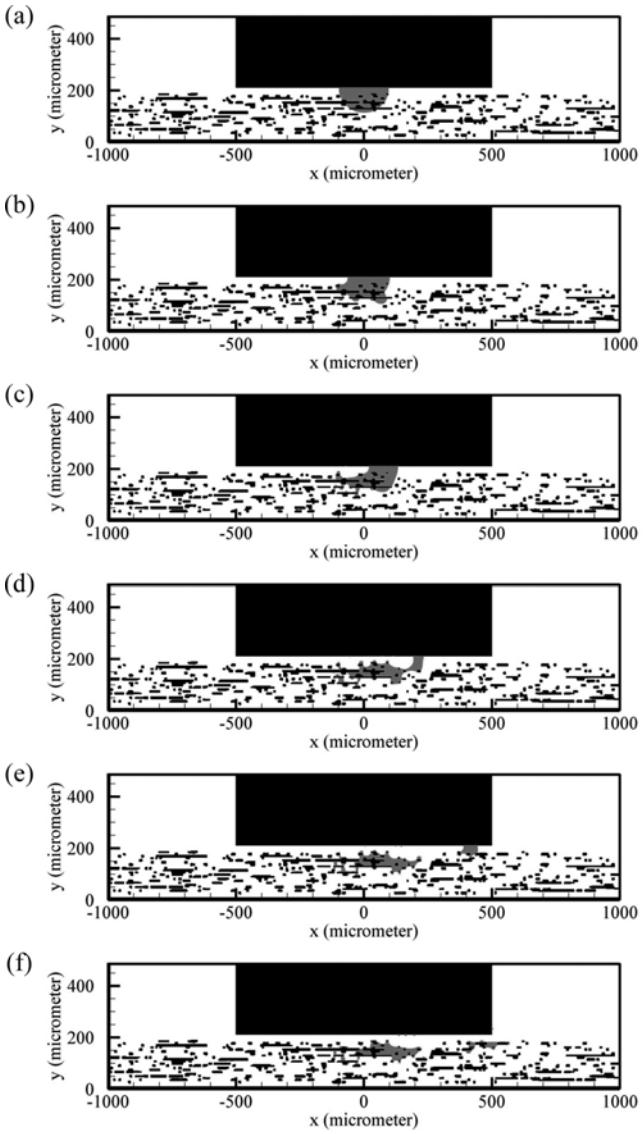

Fig. 9. Dynamic behavior of a liquid water droplet initially adhering to the land moving through the hydrophilic GDL with contact angle of 80° after: (a) 0 time steps, (b) 5000 time steps, (c) 10000 time steps, (d) 15000 time steps, (e) 20000 time steps, (f) 25000 time steps.

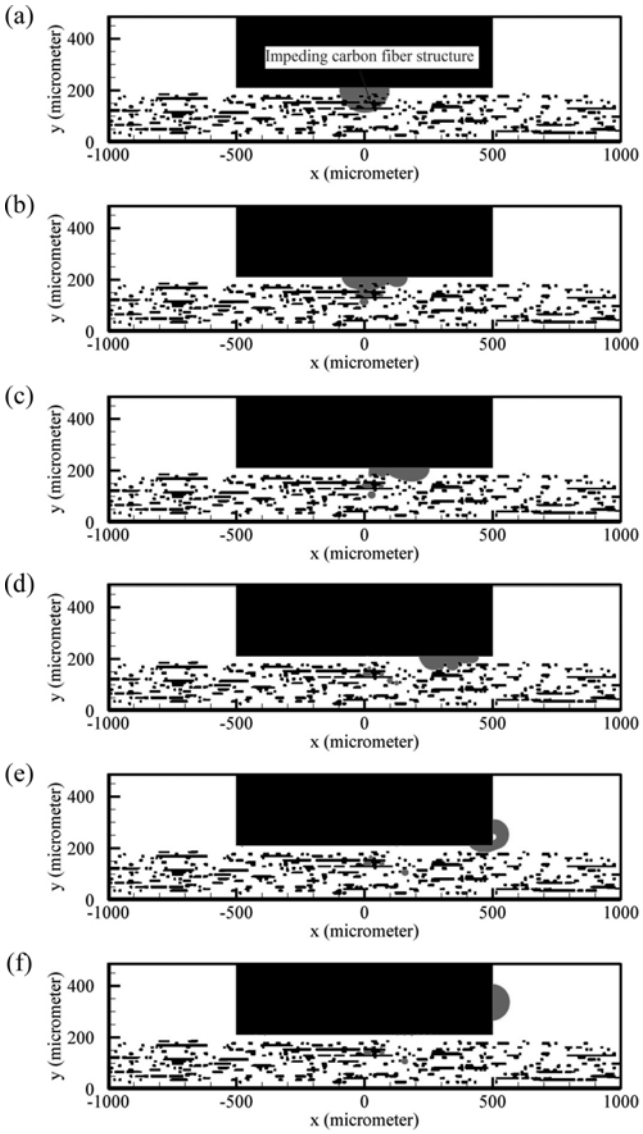

Fig. 10. Dynamic behavior of a liquid water droplet initially adhering to the land moving through the hydrophobic GDL with contact angle of 150° after: (a) 0 time steps, (b) 5000 time steps, (c) 10000 time steps, (d) 15000 time steps, (e) 20000 time steps, (f) 25000 time steps.

vapor and very small droplets from the GDL at the beginning.

1-2. Droplet Initially Adhering to the Land

The dynamic behavior of a droplet, initially adhering to the land, during removal process is shown in Fig. 9 for the hydrophilic GDL with contact angle of 80°, which represents a GDL without PTFE content. Simulation results show that the initial droplet tends to slide on the land. During sliding motion, its lower part is separated and sticks to carbon fibers. This is followed by a reconfiguration of the small sticking droplet into an aerodynamic shape that minimizes the pressure drag exerted by the gas flow. Consequently, the small droplet is stabilized such that the gas flow will be unable to remove it from its position in the GDL.

Meanwhile, the sliding portion of the initial droplet lifts off from the land and sticks to the carbon fibers close by. This seems reasonable since the land surface with a contact angle of 85° is slightly more hydrophobic than these carbon fibers. This portion also stabilizes in its position; therefore, no significant portion of the initial droplet reaches the outlet GC.

The dynamic behavior of a droplet, initially adhering to the land, during removal process is shown in Fig. 10 for the highly hydrophobic GDL with contact angle of 150°. The initial droplet easily slides on the land; this ease of movement is partly due to the hydrophobicity of the carbon fibers and partly due to their simple structure on the GDL interface. Fig. 10 shows that a small fraction of the initial droplet is trapped by an impeding carbon fiber structure just beneath the land. Due to hydrophilic nature of the land surface the sliding droplet will not lift off the land while entering the outlet GC; this stage can be seen in Fig. 10(f). The overall result of the wettability characteristics of the GDL and the land in this case is that the droplet can be easily removed from the GDL. It appears

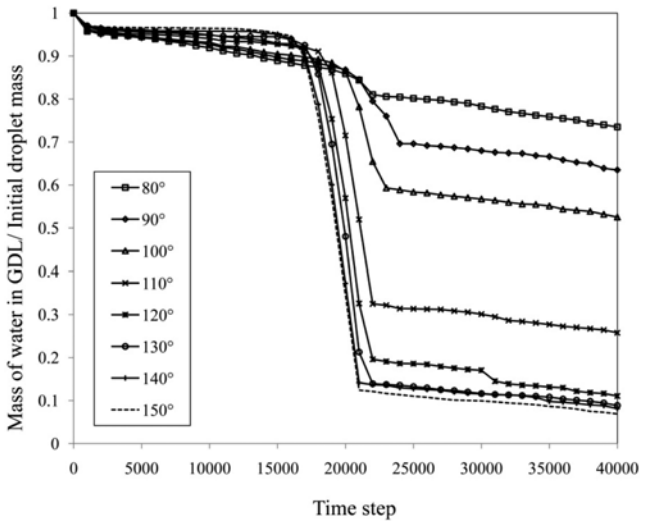

Fig. 11. The time evolution of the ratio between mass of water in the GDL and the initial droplet mass adhering to the land for the GDLs with uniform wettability (contact angles between 80° and 150°).

that when droplet initially formed on the land, the role of land wettability is crucial.

Presented in Fig. 11 is the time evolution of the ratio between mass of water in the GDL and the initial droplet mass adhering to the land, for various GDL contact angles. For the GDL contact angle of 80° the droplet cannot exit the GDL; thus no sharp reduction of water mass is seen for this hydrophilic case. As the contact angle of GDL increases, a sharp drop in the curve is observed to form sooner and steeper, which indicates exiting of more liquid water from the GDL at earlier stages. Fig. 11 also shows that the droplet behavior is not altered much for the GDL contact angles of 130° to 150°. This suggests that increasing hydrophobicity beyond a certain value would not facilitate droplet removal any more. Thus, it appears that an optimum PTFE content exists for which the best performance may be achieved [40].

2. Effect of Spanwise Gradient of Wettability

In this section water droplet removal from four different GDLs with different wettability conditions, but identical mean contact angle of 100°, is simulated to investigate the effect of spanwise gradient of wettability; one GDL is without gradient of wettability and the other three GDLs are with low, medium and high spanwise gradient of wettability as described in Fig. 5(a). It is clear that when spanwise gradient of wettability exists, the interfacial force acting on the droplet during its motion tends to move it from transverse center line (L0 in Fig. 4) towards right side line (L1 in Fig. 4).

Fig. 12 shows the dynamic behavior of a liquid water droplet, initially adhering to the MPL, during removal from the GDL with high spanwise gradient of wettability (refer to Fig. 5(a)). Since hydrophobicity of the GDL reduces from the transverse center line (the initial position of the droplet) towards the side lines (middle of the outlet gas channel), the droplet easily starts moving from its initial position. However, as the droplet moves toward the outlet GC, it slows down due to an increase in the adhesion force acting on the droplet by the carbon fibers. Interestingly, when it finally reaches the outlet GC, some hydrophilic carbon fibers prevent the droplet

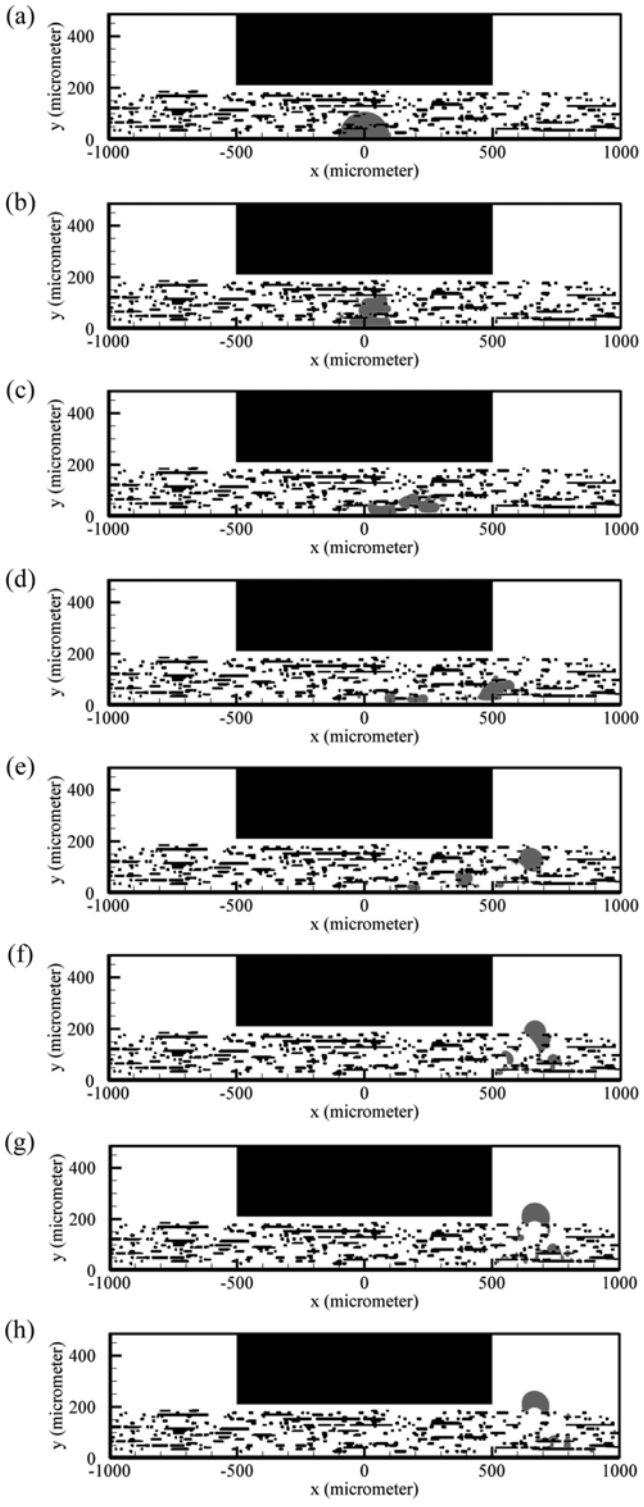

Fig. 12. Dynamic behavior of a liquid water droplet initially adhering to the MPL moving through the hydrophilic GDL with high spanwise gradient of wettability after: (a) 0 time steps, (b) 5000 time steps, (c) 15000 time steps, (d) 25000 time steps, (e) 30000 time steps, (f) 45000 time steps, (g) 55000 time steps, (h) 100000 time steps.

from moving through the channel; see Figs. 12(g)-(h).

Fig. 13 shows the dynamic behavior of a liquid water droplet, initially adhering to the land, as it moves through the GDL with

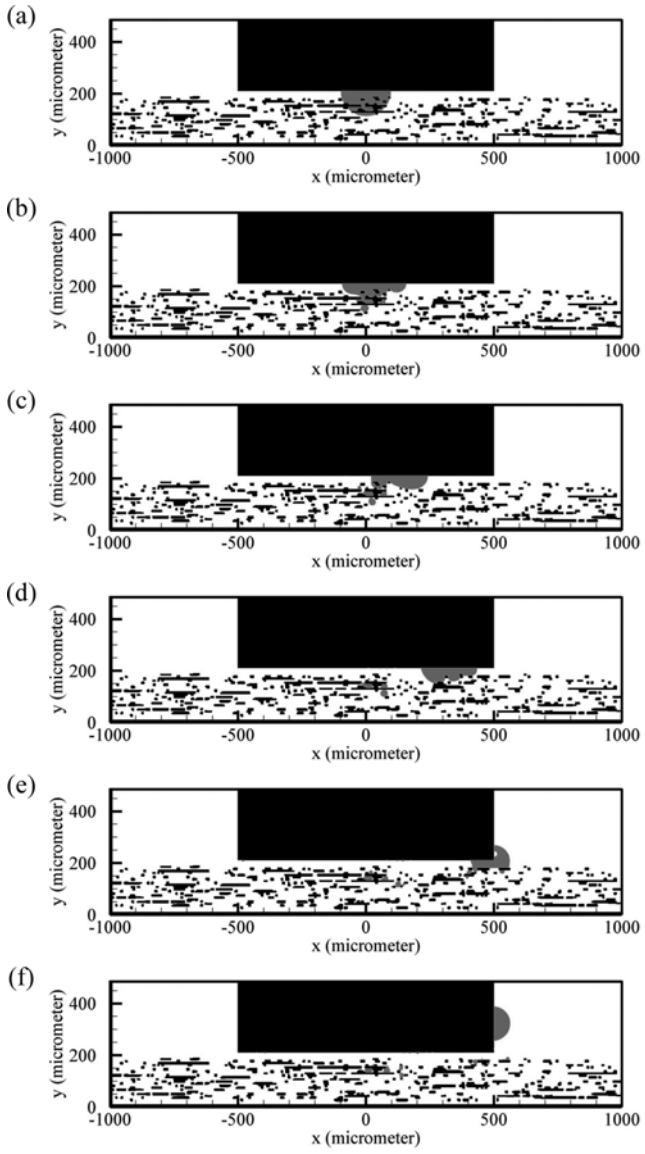

Fig. 13. Dynamic behavior of a liquid water droplet initially adhering to the land moving through the hydrophobic GDL with high spanwise gradient of wettability after: (a) 0 time steps, (b) 5000 time steps, (c) 10000 time steps, (d) 15000 time steps, (e) 20000 time steps, (f) 25000 time steps.

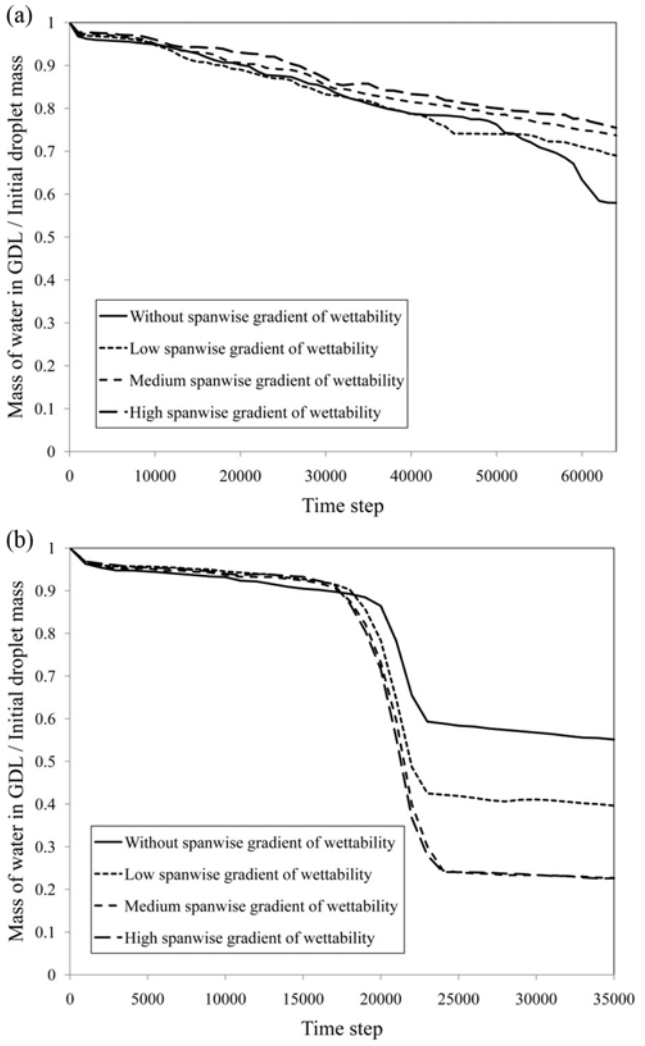

Fig. 14. The time evolution of the ratio between mass of water in the GDL and the initial droplet mass for the GDLs with different spanwise gradients of wettability: (a) droplet initially adhering to the MPL, (b) droplet initially adhering to the land.

high spanwise gradient of wettability. Similar to the previous case, the GDL contact angle reduces from 130° at the transverse center line to 70° at the side lines (refer to Fig. 5(a)). This variation result in a contact angle of 100° in the middle of these two lines (the transverse location of the outlet GC left wall). Since the contact angle at this location is greater than 90°, the droplet easily slides on the land towards the outlet GC without a difficulty.

Fig. 14 shows the time evolution of the ratio between mass of water in the GDL and the initial droplet mass during removal process for the four mentioned GDLs. For each GDL, two cases are considered where the initial droplet is placed either on the MPL or the land. The simulation results for all four GDLs with the droplet initially placed on the MPL are summarized in Fig. 14(a). It is observed that GDL's spanwise gradient of wettability will not facilitate removal of a droplet initially adhering to the MPL. Also surprisingly, increasing GDL's spanwise gradient of wettability will result in a slightly slower removal process in this case. For this particular GDL structure, the above statement can be justified as follows. The maximum transverse component of gas velocity does not occur at the centerline of the outlet GC (line L1 in Fig. 4) because of the particular microstructure of the GDL considered here. This maximum transverse component of gas velocity rather occurs somewhere between the land and centerline of the outlet GC. Hence, while the GDL's spanwise gradient of wettability pulls droplets towards the centerline of the outlet GC, it is also pulling them away from the region of maximum transverse component of gas velocity, which could otherwise readily push the droplets out of the GDL and hence facilitate water removal.

Fig. 14(b) shows that GDL's spanwise gradient of wettability will facilitate removal of a droplet initially adhering to the land (rather than to the MPL) and increasing this gradient will further enhance the removal process. This seems reasonable since by increasing GDL's

spanwise gradient of wettability, the interfacial force will push the droplet on the land more strongly towards the outlet GC. In all cases in which the droplet is initially adhering to the land, it moves through the GC while it adheres to the wall of the outlet GC.

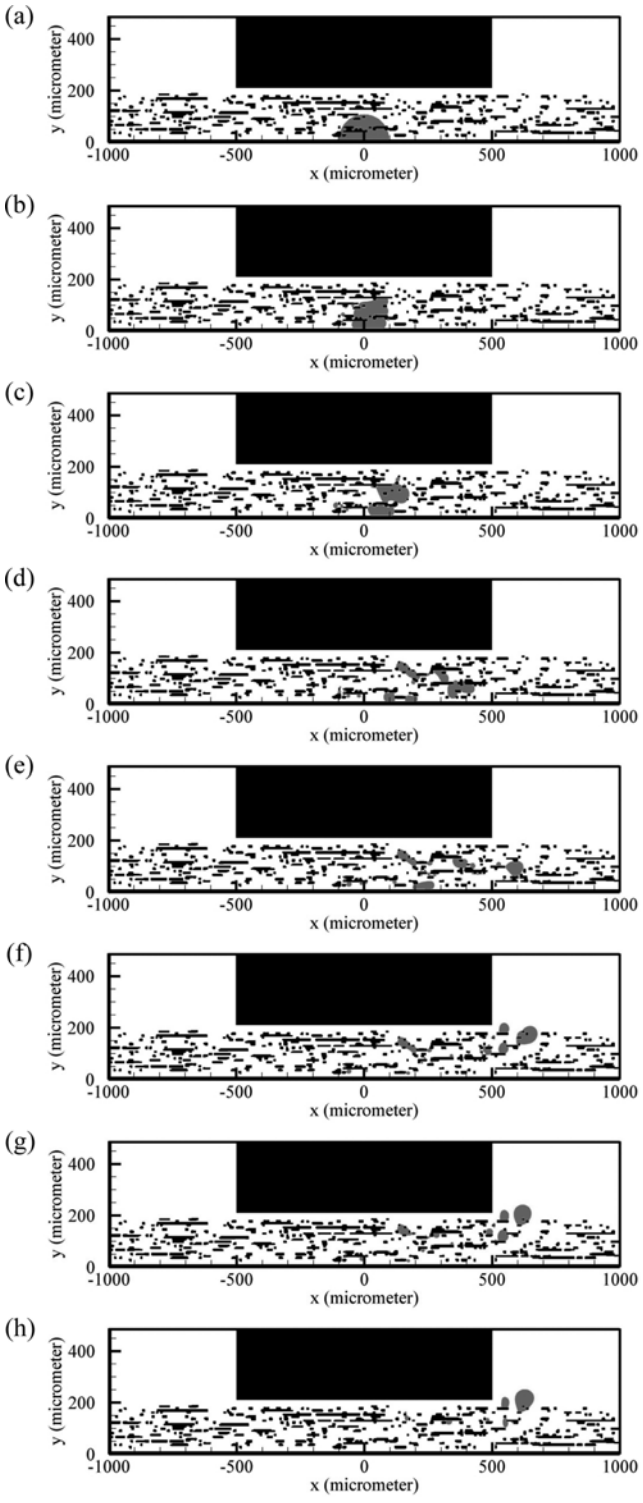

Fig. 15. Dynamic behavior of a liquid water droplet initially adhering to the MPL moving through the hydrophilic GDL with high transverse gradient of wettability after: (a) 0 time steps, (b) 5000 time steps, (c) 10000 time steps, (d) 20000 time steps, (e) 25000 time steps, (f) 35000 time steps, (g) 45000 time steps, (h) 80000 time steps.

3. Effect of Transverse Gradient of Wettability

To investigate the effect of GDL's transverse gradient of wettability on water droplet removal, simulations are conducted for four different GDLs with different wettability conditions, but with identical mean contact angle of 100°, in this section. One GDL is considered without gradient of wettability and the other three with low, medium and high transverse gradient of wettability as described previously in Fig. 5(b). It is clear that when transverse gradient of wettability exists in the GDL, the interfacial force acting on the droplet during its motion tends to move it from the bottom line (L3 in Fig. 4) towards the top line (L4 in Fig. 4).

Fig. 15 shows the dynamic behavior of a liquid water droplet, initially adhering to the MPL, moving through the GDL with high transverse gradient of wettability (refer to Fig. 5(b)). Since the hydro-

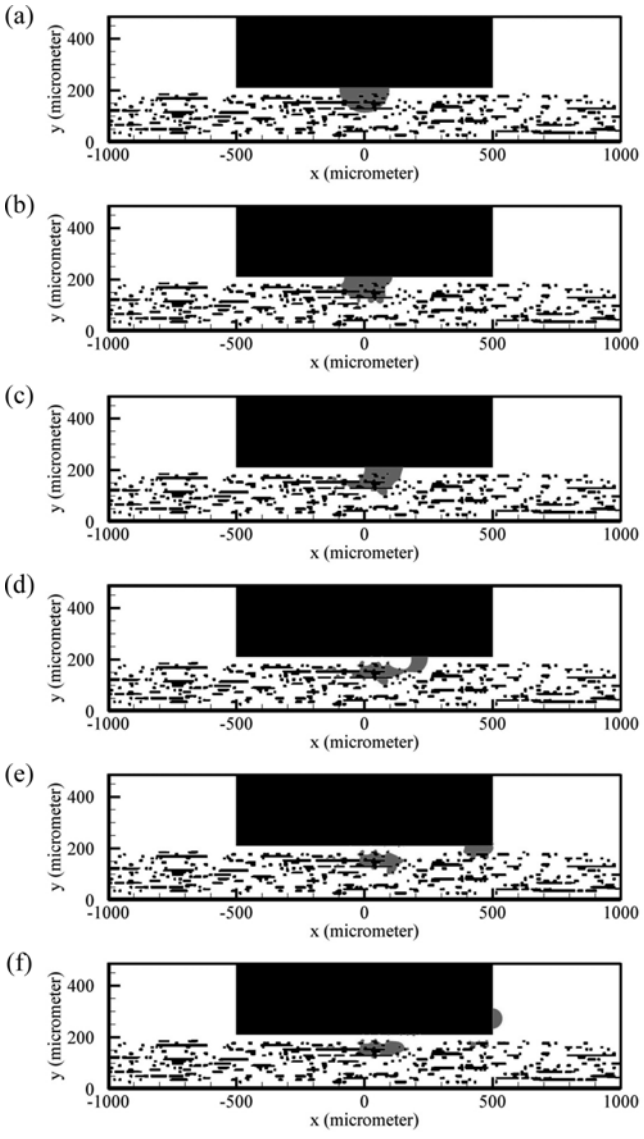

Fig. 16. Dynamic behavior of a liquid water droplet initially adhering to the land moving through the hydrophobic GDL with high transverse gradient of wettability after: (a) 0 time steps, (b) 5000 time steps, (c) 10000 time steps, (d) 15000 time steps, (e) 20000 time steps, (f) 25000 time steps.

phobicity of GDL is reduced from the bottom line (where the water droplet is initially placed) towards the top line (through which the water droplet leaves the GDL), the droplet easily starts moving from its initial position. However, due to decreasing of the contact angle during its movement towards the outlet GC, the adhesion force acting on the droplet by the carbon fibers will be increased, and hence it will slow down. Similar to the case of Fig. 12, when the droplet reaches the outlet GC some hydrophilic carbon fibers prevent it from exiting the outlet GC as shown in Figs. 15(g)-(h).

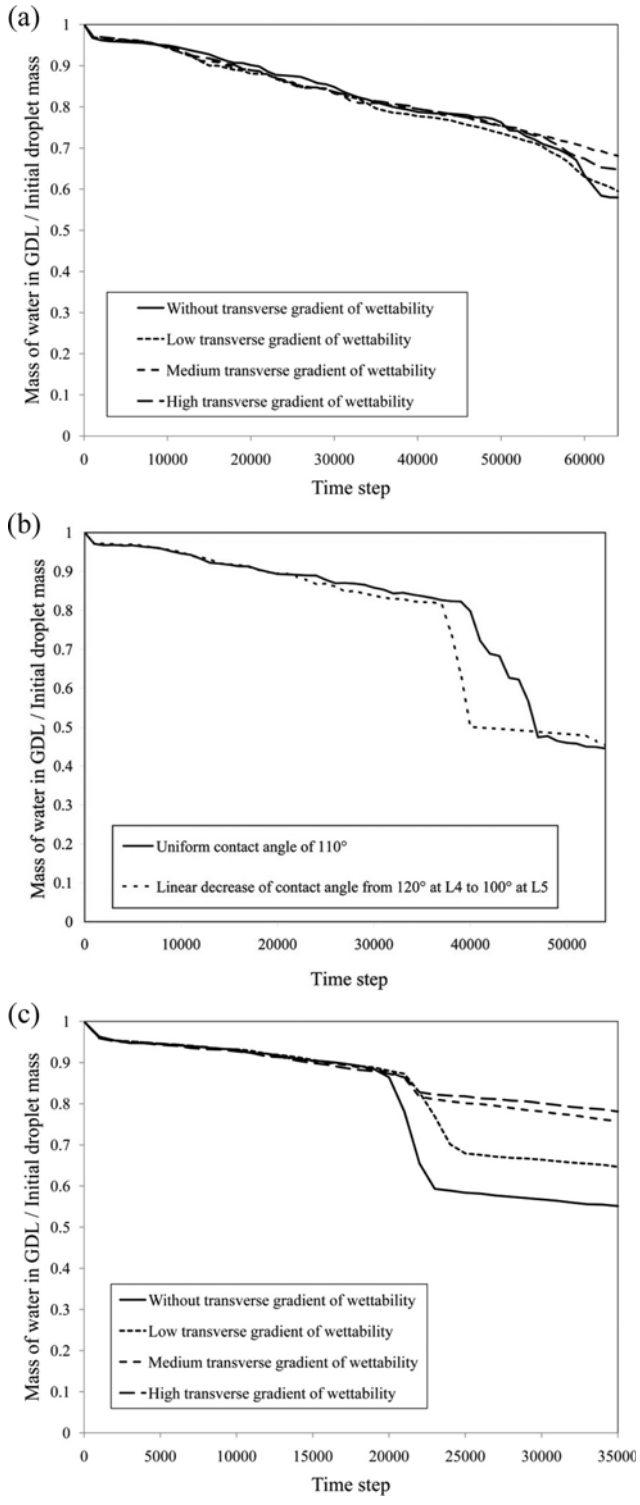

Fig. 17. The time evolution of the ratio between mass of water in the GDL and the initial droplet mass for the GDLs with different transverse gradients of wettability: (a) droplet initially adhering to the MPL with mean contact angle of 100°, (b) droplet initially adhering to the MPL with mean contact angle of 110°, (c) droplet initially adhering to the land.

Shown in Fig. 16 is the dynamic behavior of a liquid water droplet, initially adhering to the land, as it moves through the GDL with high transverse gradient of wettability (refer to Fig. 5(b)). Since the droplet must slide on the land to reach the outlet GC in this case and the carbon fibers on its path are highly hydrophilic, the largest portion of the droplet will attach to the impeding carbon fibers and only a small portion will reach the outlet GC.

Fig. 17 shows the time evolution of the ratio between mass of water in the GDL and the initial droplet mass during removal process for the four GDLs mentioned earlier. Although there is an upward interfacial force acting on the droplet during its motion through the GDL, the GDL's transverse gradient of wettability has no significant effect on the removal of a droplet if it is initially adhered to the MPL, as shown in Fig. 17(a). This is because the contact angle of GDL near the top line is less than 100°; hence when the droplet reaches the outlet GC it cannot easily detach from the GDL.

However, if the hydrophobicity of GDL decreases from the bottom line (L3 in Fig. 4) towards the top line (L4 in Fig. 4) such that the carbon fibers near the top line remain hydrophobic (for instance, decreasing contact angle from 120° at L4 to 100° at L5 with a mean value of 110°), the water droplet will be removed more easily compared to a case where the contact angle is uniformly equal to 110°; this comparison is made in Fig. 17(b).

Fig. 17(c) shows that GDL's transverse gradient of wettability will hinder removal of a droplet if initially adhering to the land, and that increasing this gradient will slow down the removal process. This can be explained as follows. Since the droplet motion in this case is through the upper layer of GDL (where it is hydrophilic), and by increasing the transverse gradient of wettability the hydrophilicity of the upper layer of GDL will increase; thus the droplet will adhere to the GDL more severely which hinders its motion.

CONCLUSIONS

The dynamic behavior of a water droplet during removal from the GDL of a PEMFC electrode with interdigitated flow field was investigated using two-dimensional LB simulations. The results of this study will be helpful to better understand the role of wettability in water removal from a PEMFC GDL. It is found that when a droplet initially adheres to the MPL, its motion through a hydrophilic GDL will involve separation into small droplets and their severe sticking to carbon fibers; on the other hand, a hydrophobic GDL will facilitate the motion of the droplet quite considerably. Also, if a droplet initially adheres to the land, it will slide on the land while moving through a hydrophilic GDL; and although some portions will be separated and stick to carbon fibers, the remained portions will easily pass the impeding carbon fiber.

Also, simulation of cases with spanwise or transverse gradient of wettability shows that decreasing hydrophobicity towards the outlet GC will lead to an interfacial force acting on the droplet that

generally eases its motion through the GDL. However, if the hydrophobicity gradient is such that the carbon fibers near the outlet GC become hydrophilic, a droplet which has reached the outlet GC will stick to carbon fibers and cannot actually exit to the outlet GC.

The main conclusions from this study can be summarized as follows:

1. Increasing the hydrophobicity of GDL (up to a threshold) will facilitate the removal of water droplet from the GDL and will also decrease the remaining mass of the initial droplet in the GDL.

2. GDL's spanwise gradient of wettability cannot improve removal of a droplet initially adhering to the MPL, while it will assist removal of a droplet initially adhering to the land.

3. The effect of GDL's transverse gradient of wettability on the removal of a droplet initially adhering to the MPL is dependent on wettability condition near the outlet GC. More specifically, if the transverse gradient of wettability is such that the carbon fibers near the outlet GC are hydrophobic, the water droplet will be removed more easily. Otherwise, the transverse gradient of wettability will hinder the removal of a droplet that initially adheres to the land.

NOMENCLATURE

$\vec{c}_i$: particle velocity in direction i of lattice [lu·ts^{-1}]
c_s : speed of sound in lattice [lu·ts^{-1}]
$\vec{F}^k_{adh}$: fluid-solid interaction force acting on a particle of type k [lm·lu·ts^{-2}]
$\vec{F}^k_{coh}$: fluid-fluid interaction force acting on a particle of type k [lm·lu·ts^{-2}]
f_i : density distribution function in direction i of lattice
f^{eq}_i : equilbrium density distribution function in direction i of lattice
f^k_i : density distribution function of component k in direction i of lattice
G^{kj}_{coh} : cohesion factor between components k and j
G^{kj}_{adh} : adhesion factor of components k to the wall
H : thickness of droplet [lu]
L : length of droplet in contact with solid surface [lu]
P : pressure [lm·lu^{-1}·ts^{-2}]
R : droplet radius [lu]
$\vec{r}$: particle position vector [lu]
s : solid function in Eq. (5)
t : time [ts]
Δt : time step [ts]
$\vec{U}$: macroscopic velocity vector [lu·ts^{-1}]
$\vec{u}^{k,eq}$: equilibrium velocity vector of component k [lu·ts^{-1}]
w_i : weighting factor for direction i of lattice

Greek Symbols

θ : static contact angle
ρ : density [lm·lu^{-3}]
σ : interfacial tension
τ : relaxation time [ts]
ψ^k : inter-particle potential function of component k

Subscripts and Superscripts

i : direction i
k : component k
ref : refrence

Abbreviations

CL : catalyst layer
DDF : density distribution function
GC : gas channel
GDL : gas diffusion layer
LBM : Lattice-Boltzmann method
MPL : micro-porous layer
PEMFC : proton exchange membrane fuel cell
PTFE : polytetrafluoroethylene
SC : Shan and Chen

REFERENCES

1. T. H. Yang, G. Park, P. Pugazhendhi, W. Y. Lee and C. S. Kim, *Korean J. Chem. Eng.*, **19**, 417 (2002).
2. J. E. Dawes, N. S. Hanspal, O. A. Family and A. Turan, *Chem. Eng. Sci.*, **64**, 2781 (2009).
3. K. Jiao and X. Li, *Prog. Energy Combust. Sci.*, **37**, 221 (2011).
4. Y. Wang, K. S. Chen, J. Mishler, S. C. Cho and X. C. Adroher, *Appl. Energy*, **88**, 981 (2011).
5. M. A. Khan, B. Sundén and J. Yuan, *J. Power Sources*, **196**, 7899 (2011).
6. S. Succi, *The lattice boltzmann equation for fluid dynamics and beyond numerical mathematics and scientific computation*, Clarendon Press, Oxford (2001).
7. Y. Gao, X. Zhang, P. Rama, R. Chen, H. Ostadi and K. Jiang, *Comput. Math. Appl.*, **65**, 891 (2013).
8. L. Hao and P. Cheng, *J. Power Sources*, **195**, 3870 (2010).
9. L. Hao and P. Cheng, *J. Heat Mass Transfer*, **53**, 1908 (2010).
10. L. Hao and P. Cheng, *Int. J. Heat Mass Transfer*, **55**, 133 (2011).
11. T. Koido, T. Furusawa and K. Moriyama, *J. Power Sources*, **175**, 127 (2008).
12. P. Mukherjee, C. Y. Wang and Q. Kang, *Electrochim. Acta*, **54**, 6861 (2009).
13. X. D. Niu, T. Munekata, S. A. Hyodo and K. Suga, *J. Power Sources*, **172**, 542 (2007).
14. Y. Tabe, Y. Lee, T. Chikahisa and M. Kozakai, *J. Power Sources*, **193**, 24 (2009).
15. Y. Ben Salah, Y. Tabe and Y. Chikahisa, *J. Power Sources*, **199**, 85 (2012).
16. Y. Ben Salah, Y. Tabe and Y. Chikahisa, *Energy Procedia*, **28**, 125 (2012).
17. L. Chen, H. B. Luan, Y. L. He and W. Q. Tao, *Int. J. Therm. Sci.*, **5**, 132 (2012).
18. B. Han and H. Meng, *J. Power Sources*, **217**, 268 (2012).
19. B. Han, J. Yu and H. Meng, *J. Power Sources*, **202**, 175 (2012).
20. L. Hao and P. Cheng, *J. Power Sources*, **190**, 435 (2009).
21. J. Park and X. Li, *J. Power Sources*, **178**, 248 (2008).
22. J. Nam and M. Kaviany, *Int. J. Heat Mass Transfer*, **46**, 4595 (2003).
23. F. Y. Zhang, X. G. Yang and C. Y. Wang, *J. Electrochem. Soc.*, **153**, A225 (2006).
24. M. M. Mench, *Fuel Cell Engines*, Wiley, New Jersey (2008).
25. M. M. Daino and S. G. Kandlikar, *Int. J. Hydrog. Energy*, **37**, 5180 (2012).

26. P. Zhou and C. W. Wu, *J. Power Sources*, **195**, 1408 (2010).
27. P. K. Sinha and C. Y. Wang, *Electrochim. Acta*, **52**, 7936 (2007).
28. P. K. Sinha and C. Y. Wang, *Chem. Eng. Sci.*, **63**, 1081 (2008).
29. S. Chen and G. D. Doolen, *Annu. Rev. Fluid. Mech.*, **30**, 329 (1998).
30. X. Shan and H. Chen, *Phys. Rev. E*, **47**, 1815 (1993).
31. P. L. Bhatnagar, E. P. Gross and M. Krook, *Phys. Rev.*, **94**, 511 (1954).
32. A. K. Gunstensen, D. H. Rothman, S. Zaleski and G. Zanetti, *Phys. Rev. A*, **43**, 4320 (1991).
33. M. R. Swift, W. R. Osborn and J. M. Yeomans, *Phys. Rev. Lett.*, **75**, 830 (1995).
34. A. A. Mohamad, *Lattice boltzmann method-fundamentals and engineering applications with computer codes*, Springer, Heidelberg (2011).
35. M. C. Sukop and D. T. Thorne, *Lattice boltzmann modeling, an introduction for geoscientists and engineers*, Springer, Heidelberg (2007).
36. P. Yuan and L. Schaefer, *Phys. Fluids*, **18**, 042101 (2006).
37. T. V. Nguyen, *J. Electrochem. Soc.*, **143**, 103 (1996).
38. Q. Zou and X. He, *Phys. Fluids*, **9**, 1591 (1997).
39. E. C. Kumbur, K. Y. Sharp and M. M. Mench, *J. Power Sources*, **168**, 356 (2007).
40. G. Velayutham, J. Kaushik, N. Rajalakshmi and K. S. Dhathathreyan, *Fuel Cells*, **7**, 314 (2007).